PHYSICAL REVIEW A **98**, 013837 (2018)

Optical chirality density and flux measured in the local density of states of spiral plasmonic structures

Aline Pham,[1] Airong Zhao,[1] Cyriaque Genet,[2] and Aurélien Drezet[1,*]
[1]*Institut NEEL, CNRS and Université Grenoble Alpes, F-38000 Grenoble, France*
[2]*ISIS, UMR 7006, CNRS-Université de Strasbourg, 67000 Strasbourg, France*

(Received 17 May 2018; published 24 July 2018)

Efforts to improve enantioselective detection of chiral molecules have initiated great interest in the fields of chiral light and chiral plasmonics. While superchiral light had been reported as highly sensitive enantiomer probes, optical response of chiral molecules can also be boosted at the vicinity of chiral plasmonic structures due to enhanced light-molecule coupling. Here, we apply the fundamental description of chiral light, known as the chirality density and flux, to the local density of states (LDOS) which rules the processes of light-matter interactions. In spiral plasmonic structures, we experimentally demonstrate the mapping of far-field chiral LDOS properties by means of polarimetry analysis. We establish the link between the degree of circular polarization of freely propagating cavity modes and the chirality density and flux. Using the reciprocity theorem, we show that this measure can be used to probe to the near-field chirality associated with surface plasmon field. By mapping the chiral features of the LDOS, we report a helpful method for guiding the design of superchiral light and for the investigation of chiral light-matter interactions, opening doors to improved chiral molecular sensing.

DOI: 10.1103/PhysRevA.98.013837

I. INTRODUCTION

Improving chirality-sensitive spectroscopy techniques remains a challenging task for pharmaceutical industry and biomolecular science. Enantiomeric discrimination relies on the fact that chiral molecules interact differently with left= and right-handed circularly polarized light, effect also known as circular dichroism (CD). However, their chiroptical response tends to be very weak, therefore, enhancing the interactions between light and chiral molecules has been the subject of intense investigation [1]. On one hand, boosted CD response in the presence of chiral metallic nanostructures has initiated great interest in the field of chiral plasmonics [2–6]. Recently, the concept of local density of states (LDOS) has been extended to chiral light-matter interactions [7] and a chiral Purcell factor has been recently introduced to characterize the enhancement of chiral molecule's spontaneous emission rate by its environment [8]. On the other hand, beyond sensitivity to circular polarization, significant enantioselectivity improvement has been demonstrated with superchiral light, thus motivating the investigation of sculpted electromagnetic fields [9–11]. With the increasing complexity of light fields, physical quantities known as the optical chirality density χ and the flux of chirality $\mathbf{\Phi}$ have been recently introduced to characterize highly twisted light [12,13]. Extensive works have investigated the physical meaning of these quantities which were shown to connect to the degree of asymmetry in the excitation rate of chiral molecules [14] and to chiral forces [15].

In this work, we connect the figures of merit of optical chirality, χ and $\mathbf{\Phi}$, to the concept of local density of states (LDOS) [16–18]. The notion of LDOS chirality can be physically interpreted as the following: chiral light-matter coupling is optimized when the emitter is positioned in areas of high LDOS chirality. Thereby the LDOS chirality helps to identify the locations of the source where its interaction with chiral cavity modes, that are sensitive to the handedness of the polarization, would be the strongest. The capacity of the cavity to "dissipate" chirality for a given position of the emitter can then be described by the LDOS chirality [19]. Supported by an in-depth theoretical analysis, we will establish the link between our optical LDOS measurements and the chirality density and flux in both far and near fields. While most methods focus on the emitter's decay rate (Purcell effect), comprehensive understanding of light-matter interaction also includes the mapping of the LDOS in momentum, space, and polarization [20,21]. Here, based on a full polarization analysis of the LDOS, we report on the experimental characterization of χ and $\mathbf{\Phi}$ in spiral plasmonic cavities, defined as canonical chiral systems. In analogy with the Poynting theorem, LDOS chirality describes the local emission and dissipation of chiral light for given positions of the emitter in a cavity. Further, to suitably engineer the coupling between chiral light and chiral molecules, both far- and near-field chirality quantities should be probed [19,22,23]. Therefore, using the reciprocity theorem [18,24], we demonstrate that far-field observables linked to LDOS polarization can describe near-field chiral properties, which connect to confined surface plasmon (SP) modes [10]. Chirality characterization of sculpted LDOS maps could then be helpful for the design of superchiral light and chiral optical forces towards improved chiral plasmonic sensors.

II. PARTIAL LDOS POLARIMETRY

Our experimental method is based on near-field scanning optical microscopy (SNOM) operating in illumination mode,

---

[*] aurelien.drezet@neel.cnrs.fr

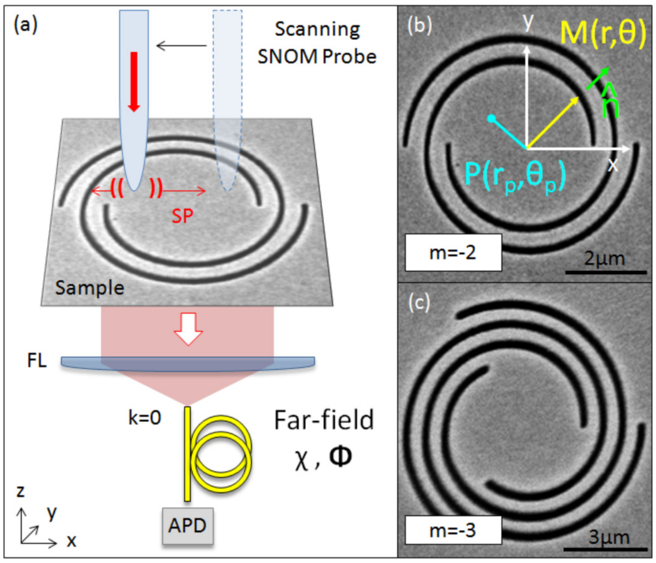

FIG. 1. (a) Experimental setup scheme. (b), (c) Scanning electron microscopy images of the plasmonic structures.

combined with a polarization tomography. It is a powerful technique to reveal spin-orbit coupling and chiral optical phenomena. Recently, this method has been used to measure the third Stokes parameter of the light scattered by an achiral nanostructure [23]. Here, we expand that conventional polarization analysis, to the general notion of the LDOS, whose significance goes beyond the measurement of light scattering. Through delocalized surface plasmons, polarimetric SNOM measurement can be extended to the combined concept of LDOS and chirality density and flux. A scheme of the optical setup is displayed in Fig. 1(a) (detailed setup is available in Appendix A): a laser beam, linearly polarized along $\hat{x}$ ($\lambda = 633$ nm), is injected into a nanoapertured optical fiber probe (typical apex diameter 100 nm) [25]. As a pointlike electric dipole, it excites propagating surface plasmons (SP) which then scatter on the grooves of the plasmonic structures [Figs. 1(b) and 1(c)]. As previously reported in [7,17], by raster scanning the sample in the xy plane, one measures the partial LDOS $\delta\rho$ pertaining to the dipole orientation $\hat{\mu} = \boldsymbol{\mu}/|\boldsymbol{\mu}|$. In the case of an aperture probe, $\hat{\mu}$ lies in the plane of the sample and is oriented according to the input laser ($\hat{\mu} = \hat{x}$). The measured partial LDOS then corresponds to the projection on the in-plane component of the dipole with respect to the sample. The radiation is collected in free space by an oil immersion microscope objective and captured by an optical fiber connected to an avalanche photodiode (APD). On one hand, whereas LDOS measurements conventionally rely on decay rate detection, momentum-resolved LDOS mapping is also crucial for engineering optical systems with directional emission [20,26–28]. The versatility of our all-optical technique allows selective recording of the optical modes associated with specific wave vectors $\mathbf{k} = k_x\hat{x} + k_y\hat{y}$ by aligning the APD collection fiber to a relevant direction of propagation. A Fourier lens is used to map the reciprocal space. The angular resolution $\delta^2 k$ is determined by the numerical aperture of the collection fiber (25-μm radius, 0.22 NA). The proof of principle is established by studying, as canonical chiral systems, spiral plasmonic cavities of different geometric charges [Figs. 1(b) and 1(c)]. Spirals are well known for producing structured fields with tailored orbital angular momentum (OAM) [29–31]. This ability is of particular interest since optical vortices have been shown to increase CD sensitivity of chiral molecules adsorbed in plasmonic nanoparticules [32]. The samples are fabricated by focused ion beam milling of a 200-nm-thick opaque gold film, evaporated on a glass substrate. In polar basis (O, r, θ), an Archimedean spiral is described by $r(\theta) = r_0 + m\lambda_{\mathrm{SP}}\frac{\theta}{2\pi}$ where $\theta \in [0; 2\pi n]$, n is the number of the spiral turns, r_0 the starting distance of the spiral, m the geometrical charge (signed integer number), and λ_{SP} the pitch taken equal to the SP wavelength to obtain resonant excitation. Here, directional LDOS measurements are carried out along the optical axis $k \approx 0 \pm \delta^2 k$, where the modes were shown to manifest chiral behavior [7]. On the other hand, the LDOS state of polarization (SOP) is characterized by a quarter wave plate and a linear polarizer which project the scattered signal onto each polarization basis $\mathbf{u}$: linear polarizations $\mathbf{X}$, $\mathbf{Y}$, $\mathbf{P}$ $(+45^\circ)$, $\mathbf{M}$ (-45°), and circular polarizations of left $\mathbf{L}$ $(s_+ = +1)$ and right-handedness $\mathbf{R}$ $(s_- = -1)$. The total scalar LDOS can be derived from $\rho(\omega, \mathbf{r}_p) = \frac{3}{\pi\omega^2|\mu|^2}P(\omega, \mathbf{r}_p)$, with $P(\omega, \mathbf{r}_p)$ the total energy rate radiated by a dipole source emitting at frequency ω and located at position $\mathbf{r}_p := [r_p, \theta_p]$ [see notations in Fig. 1(b)]. Further, efforts to investigate chiral optical phenomena have motivated the introduction of the concept of vectorial LDOS with polarization-resolved study of chiral structures [33,34]. Hence, we define the partial LDOS SOP as

$$\delta\rho^u(\mathbf{k}, \mathbf{r}_p) = \frac{3}{\pi\mu^2\omega^2}|\mathbf{E}(\mathbf{k}, \mathbf{r}_p)\cdot\mathbf{u}|^2\delta^2 k, \tag{1}$$

where the scattered field $\mathbf{E}(\mathbf{k}, \mathbf{r}_p)$ results from the interactions between the SP with the metallic grooves. The experimental $\delta\rho^u$ maps are displayed in Fig. 2. To characterize the LDOS chirality, let us start with the examination of the modes projected on the circular basis (pink frames in Fig. 2). We will demonstrate that they can be directly connected to the chirality density and flux of the cavity modes. On one hand, the data exhibit distinct salient features that confirm the ability of the spirals to spatially tune the vorticity and SOP of the light according to the geometric charge. On the other hand, $\delta\rho^{L/R}$ feature different LDOS intensity distributions. The modal profile for $m = -2$ switches from a central hot spot in $\mathbf{R}$ to a vortex mode in $\mathbf{L}$. The spiral $m = -3$ also supports spin-dependent OAM modes with a larger ring radius in the $\mathbf{L}$ basis than in $\mathbf{R}$. To understand the underlying physical mechanisms giving rise to the formation of these complex structured modes, analytical simulations are performed, based on the theoretical study introduced in [7]. By coherently summing the radiations from electric dipoles uniformly distributed along the slits $\mathbf{E}(M) \propto e^{i\mathbf{k}_{\mathrm{SP}}\cdot\mathbf{r}}/\sqrt{r}(\boldsymbol{\mu}\cdot\hat{r})\hat{r}$ (with $\hat{r} = \mathbf{r}/|\mathbf{r}|$), we deduce the expression of the scattered field propagating on the optical axis, i.e., within $\mathbf{k} \approx 0 \pm \delta^2\mathbf{k}$ (see [7] for detailed derivations):

$$\mathbf{E}(\mathbf{k}, \mathbf{r}_p) \propto \int_{\mathrm{groove}} \frac{e^{-i\mathbf{k}\cdot\mathbf{r}}}{\sqrt{r}}(\mathbf{E}(M)\cdot\hat{n})\hat{n}dl \tag{2}$$

$$= \mathbf{E}^L(\mathbf{k}, \mathbf{r}_p) + \mathbf{E}^R(\mathbf{k}, \mathbf{r}_p), \tag{3}$$

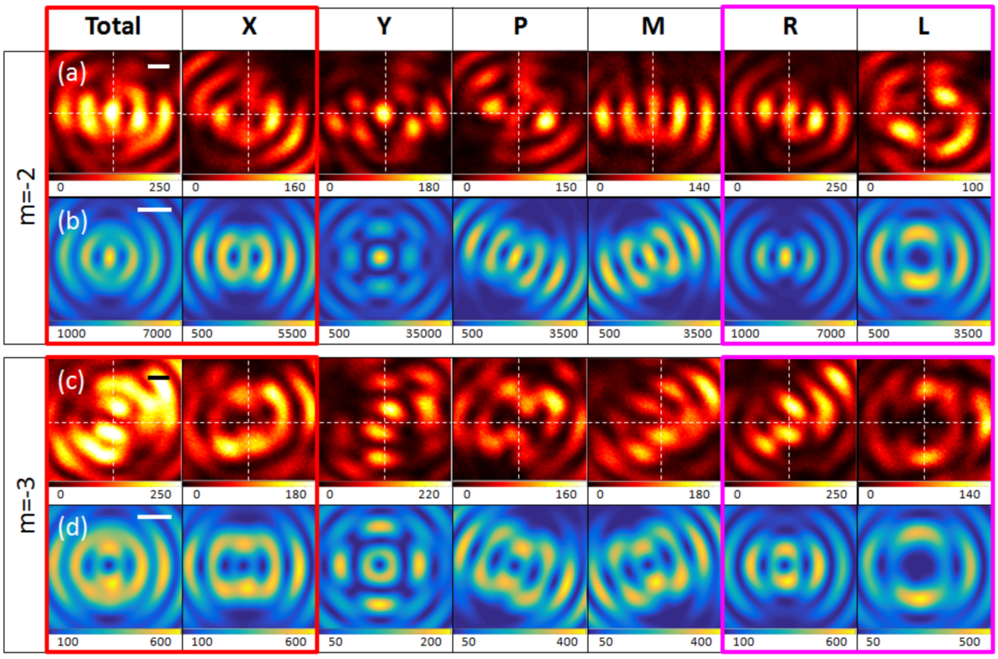

FIG. 2. Projected LDOS SOP maps: measurements and simulations in red and blue color scales, respectively [intensity (arb. units)]. Scale bar value: 500 nm.

where $\hat{n}$ is the normal to the groove at M and

$$\mathbf{E}^S(\mathbf{k},\mathbf{r}_p) \propto \sum_n \sqrt{r_n} e^{ik_{\mathrm{SP}} r_n} \{ (ie^{i\theta_p})^m J_m(V) + (ie^{i\theta_p})^{m-2s_\pm} J_{m-2s_\pm}(V) \} \mathbf{S}, \tag{4}$$

with $\mathbf{S} = \mathbf{L}$ ($s_+ = 1$) or $\mathbf{R}$ ($s_- = -1$), $V = k_{\mathrm{SP}} r_p$, and $k_{\mathrm{SP}} = 2\pi/\lambda_{\mathrm{SP}}$ the SP wave vector. Here, the mapping is carried out near the spiral center where the illumination field from the SNOM tip can be considered constant during the measurement and is not altered by the back-reflected SP (see discussion below). Since $r_0 \gg \lambda$, we made the approximation that a spiral making n turns can be described as n rings of radius $r_n = r_0 + n\lambda_{\mathrm{SP}}$. J_l stands for the Bessel function of order l (signed integer number). They are characterized by a maximum at the center when $l = 0$ and annular profiles of increasing radius with nonzero l, thus describing optical focusing and vortex modes, respectively. Analytical expressions of the partial LDOS on each SOP can then be derived from $\delta\rho^u(\mathbf{k},\mathbf{r}_p) \propto |\mathbf{E}(\mathbf{k},\mathbf{r}_p)\cdot\mathbf{u}|^2\delta^2 k$. It is described by a combination of Bessel modes whose orders are directly related to the geometrical charge m and the spin of light $s_\pm$. Specifically, the LDOS can be sculpted using an OAM selection rule which authorizes only vortices with $l = m$ and $m - 2s_\pm$. The influence of the spiral geometry on the LDOS chirality has been confirmed by probing the LDOS in a circular cavity which features insensitive response to the spin: $\delta\rho^R = \delta\rho^L$ (see Appendix B). Based on the above analytical description, the simulations shown in Fig. 2 faithfully reproduce the experimental data with a focused and dark spot in **R** and **L**, respectively, for $m = -2$. For $m = -3$, we retrieve that the LDOS in **L** corresponds to a higher-order vortex mode than in **R**. Discrepancies, such as slight tilts in the pattern orientation, are explained by experimental errors, including misalignment of the detection APD fiber with regards to the optical axis. They are also due to polarizer errors whose axis is known within ±5° uncertainties. In addition, the exciting source has been theoretically modeled as a pure in-plane dipole. However, in practice, real aperture SNOM tips could induce a slight out-of-plane dipolar excitation which has been neglected in the simulations and could contribute to the differences between the simulations and the measurements. Indeed, although the out-of-plane SP component is much stronger than the in-plane one, it has been shown previously that aperture SNOM tip mainly probes the in-plane contribution of the partial LDOS [7]. Additionally, the partial LDOS probed with a pure out-of-plane electric dipole is associated with vortex modes that strongly differ from the experimental results (for comparison, the corresponding simulations are available in Appendix C) which confirms that we can mainly focus on the in-plane LDOS contribution in this work. We should emphasize that the LDOS mapping is restricted here to paraxial propagating modes. The detection is performed in the far field, therefore, we detect only the radiative part of the LDOS.

III. FAR-FIELD LDOS CHIRALITY

Let us now turn to the examination of the chirality density χ and flux $\mathbf{\Phi}$. Although only far-field LDOS is probed here, we will see that one can extract near-field chiral property information. When χ and $\mathbf{\Phi}$ characterize radiative LDOS, i.e., freely propagating modes, they will be called far-field chirality density and flux. In contrast, we refer to near-field chirality when they describe nonradiative SP bounded to the cavity surface. We recall that these two fundamental chirality quantities are described by

$$\chi = \frac{c}{2\omega}[\boldsymbol{\mathcal{E}}\cdot\nabla\times\boldsymbol{\mathcal{E}} + \boldsymbol{\mathcal{H}}\cdot\nabla\times\boldsymbol{\mathcal{H}}], \tag{5}$$

$$\mathbf{\Phi} = \frac{c^2}{2\omega}[\boldsymbol{\mathcal{E}}\times(\nabla\times\boldsymbol{\mathcal{H}}) - \boldsymbol{\mathcal{H}}\times(\nabla\times\boldsymbol{\mathcal{E}})], \tag{6}$$

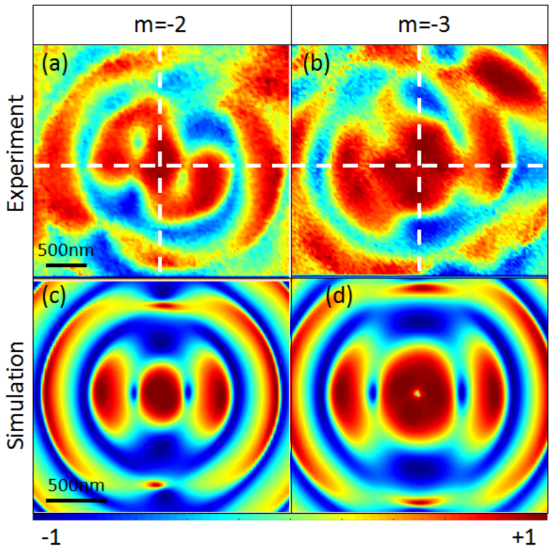

FIG. 3. Measured and simulated of S_3 maps. Color scale: $s_\pm = \pm 1$ [intensity (arb. units)].

with the real electromagnetic fields $\boldsymbol{\mathcal{E}}(\mathbf{r},t)$ and $\boldsymbol{\mathcal{H}}(\mathbf{r},t)$. Upon time averaging and in monochromatic regime, these quantities simplify to

$$\chi = \tfrac{1}{2}\mathrm{Im}(\mathbf{E}\cdot\mathbf{H}^*), \tag{7}$$

$$\boldsymbol{\Phi} = -\frac{c}{4}[\mathrm{Im}(\mathbf{E}\times\mathbf{E}^*) + \mathrm{Im}(\mathbf{H}\times\mathbf{H}^*)], \tag{8}$$

where $\boldsymbol{\mathcal{E}}(\mathbf{r},t) = \mathrm{Re}\{[\mathbf{E}(\mathbf{r})e^{-i\omega t} + \mathbf{E}^*(\mathbf{r})e^{i\omega t}]/2\}$ and $\boldsymbol{\mathcal{H}}(\mathbf{r},t) = \mathrm{Re}\{[\mathbf{H}(\mathbf{r})e^{-i\omega t} + \mathbf{H}^*(\mathbf{r})e^{i\omega t}]/2\}$ (Im and Re refer to the imaginary and real parts, respectively). Characterizing these quantities are highly relevant since they were shown to relate to chiral forces and to describe differential absorption of circularly polarized light in chiral materials [12,13,15,19].

Let us derive the expressions of far field χ and $\boldsymbol{\Phi}$ induced in the spiral cavities. Since the LDOS maps were recorded along the optical axis and the variation of the field envelope is slow within the distance λ, it is then suitable to consider the paraxial regime such that $\mathbf{H} = \hat{z} \times \mathbf{E}$. In the paraxial regime, the chirality density and flux then write as

$$\chi = -\frac{1}{2}\mathrm{Im}(\mathbf{E}\times\mathbf{E}^*)\cdot\hat{z} = -\frac{S_3}{2}, \tag{9}$$

$$\boldsymbol{\Phi} = -\frac{c}{2}\mathrm{Im}(\mathbf{E}\times\mathbf{E}^*)\cdot\hat{z} = c\chi\hat{z} = -c\frac{S_3}{2}\hat{z}, \tag{10}$$

where $S_3 = |\mathbf{E}\cdot\mathbf{L}|^2 - |\mathbf{E}\cdot\mathbf{R}|^2 \propto (\delta\rho^{\mathbf{L}} - \delta\rho^{\mathbf{R}})$ refers to the third Stokes parameter applied to the LDOS. Thereby, this result establishes the link between the measured LDOS and the chirality, hence, the capacity of the cavity to dissipate chirality for a given position of the emitter. Physically, the expansion of standard $S3$ measurement to the general notion of LDOS describes the positions of the emitter for which its probability to emit in the left or right circular polarization is the highest. Here, the measurements presented in Fig. 3 show that the coupling to the left circularly polarized modes of the cavity is maximum if the emitter is placed at the center or in the lateral lobes represented in red. Remarkably, we find that both quantities χ and $\boldsymbol{\Phi}$ are physically measurable and are proportional to the degree of circular polarization. While experimentally based on conventional polarization tomography, we underline that the proposed method goes beyond the standard $S3$ measurement of scattered light but expands to the general notion of LDOS. In analogy with the Poynting's theorem, it can be physically understood as the following: the radiation from the dipole emitter is linearly polarized thus has initially a zero chirality flux ($S_3 = 0$). As it interacts with a chiral system, chirality density can dissipate such that an optical response sensitive to $\mathbf{R}$ and $\mathbf{L}$ is induced ($S_3 \neq 0$). It leads to a nonzero outgoing chirality flux. The measured S_3 maps shown in Figs. 3(a) and 3(b) then characterize χ and $\boldsymbol{\Phi}$ associated with the spiral structures $m = -2$ and -3. They exhibit a central hot spot of left-handedness surrounded by two lateral lobes. They define the positions of the source for which the probability of chirality dissipation into the modes $\mathbf{L}$ is the highest. These main patterns are retrieved in the theoretical simulations [Figs. 3(c) and 3(d)]. Based on the OAM selection rule governing the Bessel modes, we demonstrate that χ and $\boldsymbol{\Phi}$ can be shaped via the spiral geometric charge. Thereby, we have provided an unprecedented experimental measure of both chirality density and flux applied to the LDOS. In a complementary manner to the chiral Purcell factor, which characterizes the emission enhancement of chiral molecules, the LDOS chirality density and flux describe the optimum positions at which emitters would dissipate chirality into a given cavity mode. This might be used as guidelines for positioning emitters in cavities towards nanoscale superchiral light sources.

IV. NEAR-FIELD CHIRALITY

To establish the link between far- and near-field chirality density and flux, we now consider a theoretical reciprocal setup in which the illumination and detection are swapped [Fig. 4(a)]: the sample is excited from the substrate side while the SNOM probe is used in collection mode. The whole sample is illuminated with a collimated beam ($k = 0$) with $\mathbf{X}$ polarization, i.e., the dominant channel in the experiment [Fig. 1(a)]. Indeed, in SNOM illumination mode, the SP propagate according to the dipole orientation $\hat{\mu} = \hat{x}$ then efficiently scatter into $\mathbf{X}$-polarized free-space radiation. This is confirmed in Fig. 2 (red frames) where a strong similarity between the partial LDOS without polarization analysis (first column) and $\delta\rho^X$ maps (second column) suggests that $\mathbf{X}$-polarized modes dominate in the far field. By applying the reciprocity theorem, the cavity is then excited with that predominant mode $\mathbf{X}$. In the reciprocal configuration, it scatters on the groove, induces SP which propagate towards the spiral center where they interfere. The resulting dominant SP mode in reciprocal illumination can be described in terms of in-plane and out-of-plane components such as [35]

$$\mathbf{E}_{\mathrm{SP}}(\mathbf{r}) = \mathbf{E}_{\mathrm{SP}}^{\parallel}(\mathbf{r}) + \mathbf{E}_{\mathrm{SP}}^{\perp}(\mathbf{r}), \tag{11}$$

$$\mathbf{H}_{\mathrm{SP}}(\mathbf{r}) = \frac{k}{k_z}\hat{z} \times \mathbf{E}_{\mathrm{SP}}^{\parallel}(\mathbf{r}). \tag{12}$$

Now, to detect the in-plane SP field $\mathbf{E}_{\mathrm{SP}}^{\parallel}(\mathbf{r}_p)$, the SNOM probe is scanned near the position $\mathbf{r}_p$. It is expressed in circular basis

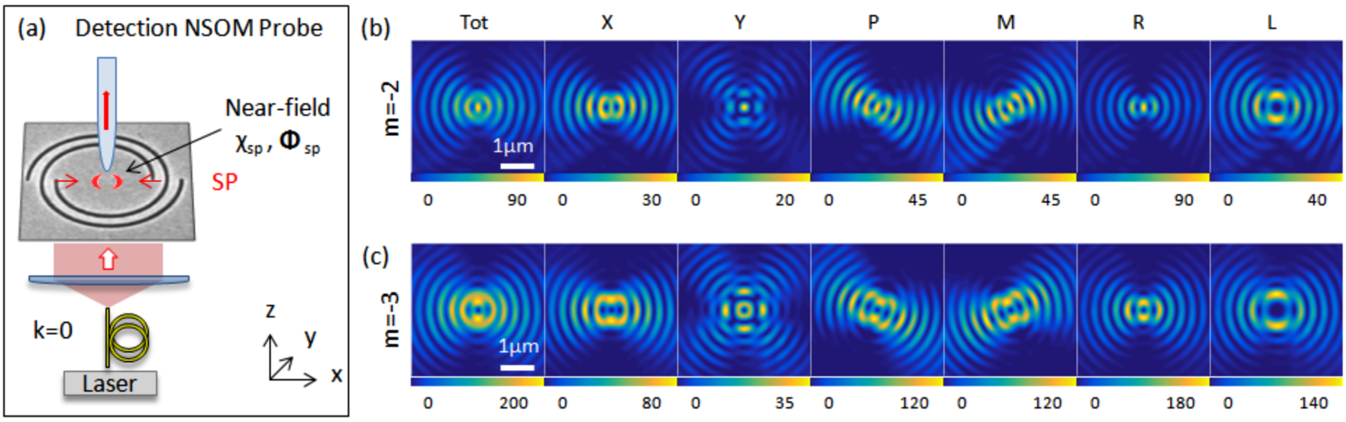

FIG. 4. (a) Scheme of the reciprocal optical setup. (b), (c) Simulations of $|\mathbf{E}^{\parallel}_{\mathrm{SP}}\cdot\mathbf{u}|^2$ (**u**=**X**, **Y**, **P**, **M**, **R**, **L**) for spiral cavities of (b) $m=-2$, (c) $m=-3$. Color scale: intensity (arb. units).

S=**R**, **L** as

$$\mathbf{E}^{\parallel,S}_{\mathrm{SP}}(\mathbf{r}_p)\propto\sum_n\frac{\mu}{4\pi\sqrt{2}}\sqrt{r_n}e^{ik_{\mathrm{SP}}r_n}\{(ie^{i\theta_p})^m J_m(V) + (ie^{i\theta_p})^{m-2s_\pm}J_{m-2s_\pm}(V)\}\mathbf{S}. \tag{13}$$

On one hand, the equivalence between Eqs. (4) and (13) corroborates our partial LDOS measurements: the field predicted by the reciprocal setup [Fig. 4(a)] exhibits the same Bessel modes as the partial LDOS maps reconstructed experimentally with the setup Fig. 1(a). Details on the derivations can be found in Appendix D. The intensity maps of $|\mathbf{E}^{\parallel}_{\mathrm{SP}}\cdot\mathbf{u}|^2$ are shown in Figs. 4(b) and 4(c) (**u** refers to the SOP vector). They correspond to the field that a collection SNOM fiber should map when scanned at the vicinity of the spiral center. We indeed verify that the in-plane SP fields are described by similar Bessel modes as in Fig. 2. Therefore, we deduce that the measured LDOS maps effectively describe the locations of the emitter where the coupling to circular polarized modes is maximized. Importantly, the knowledge of far-field LDOS helps to describe the main features of the near-field SP field.

On the other hand, it is worth noticing that $\mathbf{H}_{\mathrm{SP}}$ [Eq. (12)] and $\mathbf{H}=\hat{z}\times\mathbf{E}$ (paraxial regime) exhibit similar dependence with respect to the electric field, which suggests the link between far- and near-field chiral properties. A recent theoretical study reported that $\mathbf{\Phi}$ can be used as a far-field probe for near-field chirality in lossy dispersive media [19]. Here, we report on its experimental demonstration. In the present case, near-field chirality is linked to the SP modes confined at the cavity surface and are denoted as χ_{SP} and $\mathbf{\Phi}_{\mathrm{SP}}$. First, we find that the chirality density arising from a reciprocal illumination is given by

$$\chi_{\mathrm{SP}}=-\frac{k}{2}\mathrm{Im}\left\{\frac{(\mathbf{E}^{\parallel}_{\mathrm{SP}}\times\mathbf{E}^{*\parallel}_{\mathrm{SP}})}{k_z}\cdot\hat{z}\right\}. \tag{14}$$

Alike far-field χ [Eq. (10)], χ_{SP} is also described, up to a factor k_z, by the imaginary part of the vectorial product of the field. Additionaly, due to the equivalence between **E** [Eq. (4)] and $\mathbf{E}^{\parallel}_{\mathrm{SP}}$ [Eq. (13)] (reciprocity theorem), we can then infer that χ linked to the radiative LDOS also provides crucial information on χ_{SP} for nonradiative SP field. As far as the SP chirality flux is concerned, we derive its out-of-plane and in-plane components $\mathbf{\Phi}_{\mathrm{SP}}=\mathbf{\Phi}^{\perp}_{\mathrm{SP}}+\mathbf{\Phi}^{\parallel}_{\mathrm{SP}}$ such as

$$\mathbf{\Phi}^{\perp}_{\mathrm{SP}}=-\frac{c}{4}\mathrm{Im}\left\{(\mathbf{E}^{\parallel}_{\mathrm{SP}}\times\mathbf{E}^{*\parallel}_{\mathrm{SP}})\left[1+\left(\frac{k}{k_z}\right)^2\right]\right\}, \tag{15}$$

$$\mathbf{\Phi}^{\parallel}_{\mathrm{SP}}=-\frac{c}{2}\mathrm{Im}\{\mathbf{E}^{\parallel}_{\mathrm{SP}}\times\mathbf{E}^{*\perp}_{\mathrm{SP}}\}. \tag{16}$$

The knowledge on $\mathbf{E}^{\parallel}_{\mathrm{SP}}$ (thus **E**) provides again a complete description of $\mathbf{\Phi}^{\perp}_{\mathrm{SP}}$, thus pointing out the strong similarity between far-field $\mathbf{\Phi}$ [Eq. (10)] and near-field $\mathbf{\Phi}^{\perp}_{\mathrm{SP}}$, up to a constant $1+(\frac{k}{k_z})^2$. By mapping the far-field LDOS, one can deduce the main spatial distribution of the chirality density and on-axis flux linked to the SP. We should be precise that the determination of the transverse component $\mathbf{\Phi}^{\parallel}_{\mathrm{SP}}$ requires the mapping of $\mathbf{E}^{\perp}_{\mathrm{SP}}$ which is not probed here. For the sake of completeness, we point out that χ_{SP} and $\mathbf{\Phi}_{\mathrm{SP}}$ relate to the SP field which has to be distinguished from the total LDOS that includes radiative and nonradiative interactions with the cavity. In the following study, we will demonstrate that they lead to distinct optical vortices, which further support the validity of our chirality measurement.

V. BACK-REFLECTED FIELD TO THE DIPOLE SOURCE

The total LDOS can be deduced from the power radiated by the dipole on itself [18,24] and would account for the SP field reflected back to the dipole emitter. In Fig. 5, we illustrate the different steps leading to the reflection of SP back on the dipole emitter: (1) The illumination SNOM probe excites propagating SP. (2) The SPs scatter on the grooves and induce in turn an in-plane dipole normal to the slit [31,35]. (3) Finally, the SP field is back-reflected to emitter position. By summing the contribution from all the point sources distributed along the grooves, the total back-reflected SP field $\mathbf{E}^{\parallel}_{\mathrm{SP}}(P)=\mathbf{E}^{\parallel,R}_{\mathrm{SP}}(P)+\mathbf{E}^{\parallel,L}_{\mathrm{SP}}(P)$ writes as

$$\mathbf{E}^{\parallel,S}_{\mathrm{SP}}(P)\propto\sum_n\frac{\mu}{4\pi\sqrt{2}}\sqrt{r_n}e^{i2k_{\mathrm{SP}}r_n}\{(ie^{i\theta_p})^{2m}J_{2m}(2V) + (ie^{i\theta_p})^{2(m-s_-)}J_{2(m-s_\pm)}(2V)\}\mathbf{S}, \tag{17}$$

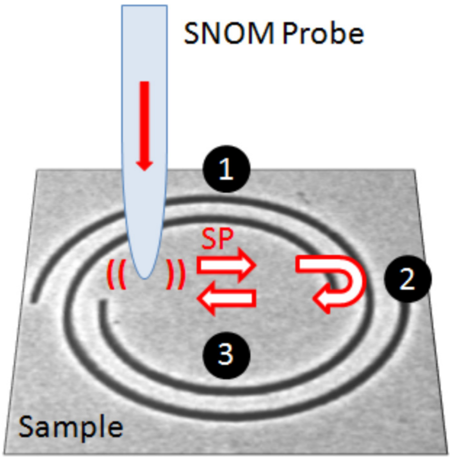

FIG. 5. Illustration of the mechanism of the SP generated and SP back-reflected to the emitter dipole.

The detailed derivations can be found in Appendix E. Equation (17) demonstrates that the total LDOS is governed by a distinct OAM selection rule which now allows only Bessel modes with $l = 2m$ and $2(m - s_\pm)$. They are fundamentally different from those found in Eqs. (4) and (13). On one hand, the contradiction between Eqs. (17) and (13) supports our previous results: when applying the reciprocal theorem, one characterizes the chirality of the in-plane component of surface plasmons which has to be distinguished from the total LDOS chirality.

On the other hand, this result highlights the influence the field existing at the edges of the nanostructure and confirms the validity of our optical setup to map the optical LDOS. Indeed, as our experimental data strongly differ from the optical vortex predicted in Eq. (17), we can conclude that the SNOM emission is not affected by the back-reflection of the SPs. Therefore, the emitter field can be considered constant during the measurement at $r_p = 0$ [24,36]. Our work dramatically differs from [23] which focuses on localized SP so the SNOM emission can be disrupted by the SP. In summary, our work has thus revealed that crucial features of the near-field chirality can be captured from far-field polarization measurements of the partial LDOS.

VI. LDOS POLARIMETRY

Furthermore, beyond enantioselective sensing applications, a comprehensive knowledge of the LDOS associated with vectorial vortex is also predicted to hold great potentials in the generation of polarized structured beams [37–40] with controlled directionality [41,42]. Polarization response of nanospiral has also been investigated for the generation of nonlinear optical effects [43]. Spatial reconstruction of the LDOS vectorial properties is deduced from the four Stokes parameters: $S_0 \propto \delta\rho^X + \delta\rho^Y$, $S_1 \propto \delta\rho^X - \delta\rho^Y$, $S_2 \propto \delta\rho^P - \delta\rho^M$, and $S_3 \propto \delta\rho^L - \delta\rho^R$. The polarization ellipse characteristics, i.e., its ellipticity ε, orientation β, and handedness $s_\pm$, are then calculated using $\sin(2\varepsilon) = S_3/S_0$, $\tan(2\beta) = S_2/S_1$, and $s_\pm = \mathrm{sgn}(S_3)$. We juxtapose to the LDOS vortex intensity maps the vector field which can be identified at each point in space (Fig. 6). This representation provides an immediate and qualitative visualization of the sculpted modes simultaneously with the inhomogeneous polarization. Specifically, by following the variations of ε, one can track both far- and near-field χ and $\mathbf{\Phi}$ evolution according to the intensity of the LDOS. Thereby, one can determine the dipole positions for which both emission probability and chirality dissipation are high. The local LDOS SOP featured in each lobe patterns can be identified and show good qualitative agreement with the simulations. For $m = -2$, the central hot spot features indeed nearly left-handed circular polarization, evolving from **X** to **R** in the side lobes. For $m = -3$, we recover a minimum intensity at the center with left-handed polarization surrounded by two hot spots. The proposed approach then bears great opportunities in nanophotonics as the evolution of ε, β, and $s_\pm$ according to emitter position can be precisely monitored in space. By enabling the mapping of far- and near-field chirality, our methodology can raise practical possibilities in the engineering of suitable chiral light-molecules coupling.

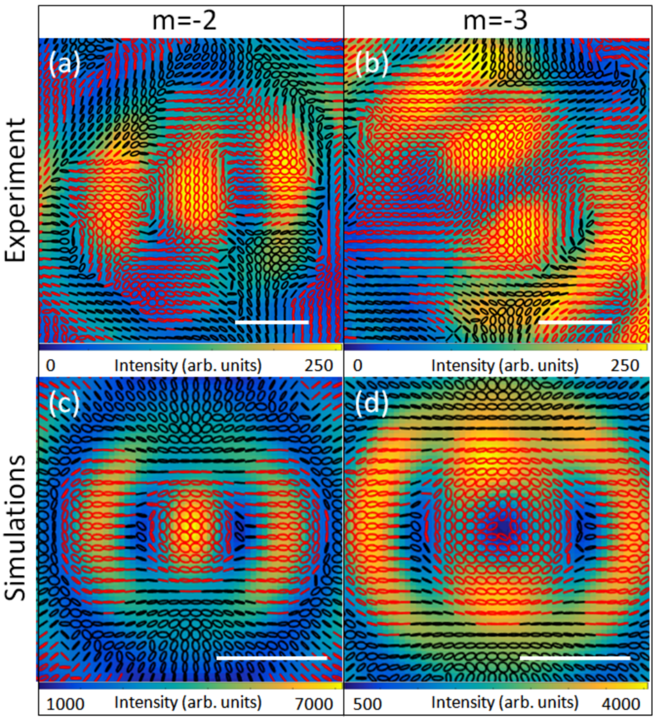

FIG. 6. Experimental and theoretical LDOS field maps. Polarization ellipses are superimposed on the LDOS total intensity: red and black lines refers to s_+ and s_-, respectively. Scale bar value: 500 nm.

To conclude, we connect the measure of optical chirality to the concept of LDOS. By probing the LDOS polarization and applying the reciprocity theorem, we demonstrate that the degree of circular polarization can describe both far- and near-field chirality in spiral plasmonic cavities. We reveal that far-field LDOS can be used as an observable for probing near-field SP chirality. The proposed method could be used as guidelines for positioning molecules in a cavity to the optimum channel of emission and chirality dissipation. Aside from applications in enantiomeric discrimination, mapping of vectorial vortex LDOS could benefit to the investigation of novel light-matter interactions relevant optical manipulation [44–46] and optical communications [47].

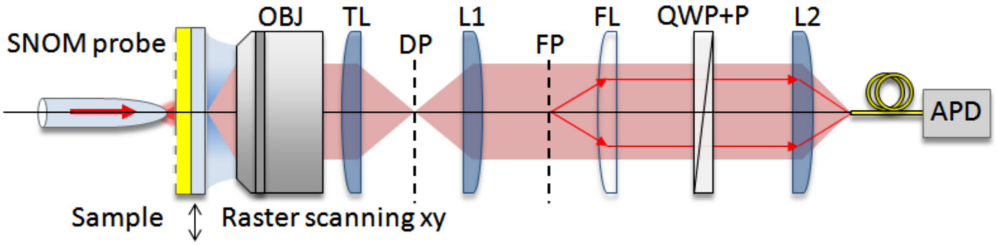

FIG. 7. Experimental optical setup.

ACKNOWLEDGMENTS

This work was supported by Agence Nationale de la Recherche (ANR), France, through SINPHONIE Grant No. ANR-12-NANO-0019 and PLACORE Grant No. ANR-13-BS210-0007. C.G. also thanks the financial support from ANR Equipex Union (Grant No. ANR-10-EQPX-52-01), the Labex NIE projects (Grant No. ANR-11-LABX-0058-NIE). The Ph.D. grant of A. P. by the Ministère de l'enseignement et la recherche scientifique, of A. Z. by the China Scholarship Council are gratefully acknowledged. We thank J.-F. Motte and G. Julie, from NANOFAB facility in Neel Institute, for the sample fabrication.

APPENDIX A: EXPERIMENTAL SETUP

Detailed sketch of the experimental setup is displayed in Fig. 7: a linearly polarized laser beam is injected into the SNOM aperture probe. The scattered signal is collected by a microscope objective (OBJ). DP stands for direct plane. A Fourier lens (FL) enables to image the back focal plane (FP). The signal is collected by an optical fiber connected to an avalanche photodiode (APD). To map the partial LDOS, we record the signal in the FP while the SNOM tip is scanned over the sample. The APD is maintained at fixed position $k = 0$. Polarimetry analysis is achieved by means of a quarter wave plate (QWP) and a polarizer (P).

APPENDIX B: CIRCULAR PLASMONIC CAVITY

In Fig. 8, we display the measurements and simulations associated with a circular plasmonic cavity.

APPENDIX C: OUT-OF-PLANE PARTIAL LDOS

When the cavity is probed by an electric dipole with an out-of-plane orientation $\boldsymbol{\mu} = \mu\hat{r}$, the partial LDOS is given by $\delta\rho_\perp(k \approx 0, \mathbf{r}_p) = \delta\rho_\perp^L + \delta\rho_\perp^R$ with

$$\delta\rho_\perp^S(\mathbf{k} \approx 0, \mathbf{r}_p) \propto \left| \sum_n \mu\sqrt{r_n}e^{ik_{\mathrm{SP}}r_n} \right|^2 J^2_{m+s_\pm}(V), \tag{C1}$$

with $V = k_{\mathrm{SP}}r_p$ and $\mathbf{S} = \mathbf{L}$ or $\mathbf{R}$. The simulated maps for spiral cavities with $m = -2$ and -3 show LDOS patterns that strongly differ from the measurements (Fig. 9). This is explained by the fact that the partial LDOS is described by distinct Bessel modes in the case of an in-plane ($l = m$ and $m + 2s_\pm$) and out-of-plane ($l = m + s_\pm$) dipole excitation.

APPENDIX D: IN-PLANE PLASMONIC FIELD IN RECIPROCAL CONFIGURATION

Here, we provide the detailed calculations for the in-plane SP field in reciprocal configuration [Fig. 4(a)]. We recall that SP propagating along air and metal interface (at $z = 0$) are transverse magnetic waves which are defined by the electric and magnetic fields such as $\mathbf{E}_{\mathrm{SP}} = \nabla\times\nabla\times(\Psi\hat{z}) = \mathbf{E}_{\mathrm{SP}}^{\parallel} + \mathbf{E}_{\mathrm{SP}}^{\perp}$ and $\mathbf{H}_{\mathrm{SP}} = -ik\nabla\times(\Psi\hat{z})$. $\parallel$ and $\perp$ refer to the in-plane and out-of-plane field components with respect to the sample. They are given by

$$\mathbf{E}_{\mathrm{SP}}^{\parallel} = ik_z\nabla_\parallel\psi, \tag{D1}$$

$$\mathbf{E}_{\mathrm{SP}}^{\perp} = k_{\mathrm{SP}}^2\psi\hat{z}, \tag{D2}$$

$$\mathbf{H}_{\mathrm{SP}} = \frac{k}{k_z}\hat{z}\times\mathbf{E}_{\mathrm{SP}}^{\parallel}, \tag{D3}$$

where $\Psi(x,y,z) = \psi(x,y)e^{ik_z z}$ is the Debye function verifying the Helmholtz equation and $k^2 = k_{\mathrm{SP}}^2 + k_z^2$. The spiral is illuminated as depicted in Fig. 4(a) with a collimated beam polarized along $\mathbf{X}$. Propagating SP are produced as a result of the scattering of the illumination beam on the grooves. The induced radiation at point M writes $\mathbf{E}(M) \propto (\boldsymbol{\mu}\cdot\hat{n})\hat{n} = \mu\cos(\theta)\hat{n}$, with $\hat{n}$ the normal to the slit. The total in-plane SP

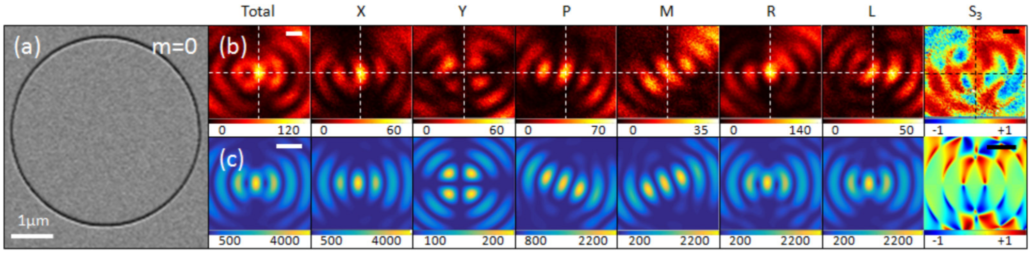

FIG. 8. (a) SEM image of the circular plasmonic cavity. (a) Experimental LDOS data. (b) Simulations LDOS data. Scale bar value: 500 nm. Color scales: intensity (arb. units).

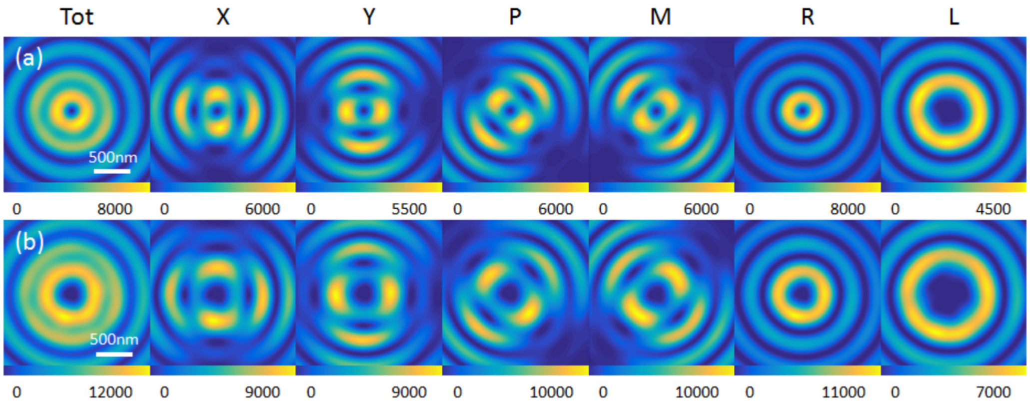

FIG. 9. Simulations of the partial LDOS projected on the orientation of a pure out-of-plane dipole in spiral cavities of (a) $m = -2$, (b) $m = -3$. Color scales: intensity (arb. units).

field at P is then calculated by summing the contribution of all the point sources distributed along the grooves (see notations in Fig. 10):

$$\mathbf{E}(P) \propto \int_{\theta_0}^{\theta_0+2\pi n} \frac{e^{ik_{\mathrm{SP}}\cdot r}}{r} (\mathbf{E}(M)\cdot\hat{n})(\hat{n}\cdot\hat{r})\hat{r}\,dl. \tag{D4}$$

We consider a tip position P at the vicinity of the spiral center. As $r_0 \gg \lambda_{\mathrm{SP}}$, it is suitable to approximate a spiral making n turns as n concentric rings of radius $r_n = r_0 + n\lambda_{\mathrm{SP}}$. Moreover, we assume $\hat{r} \approx \hat{n} \approx \mathbf{PM}/|\mathbf{PM}|$ and $k_{\mathrm{SP}}\cdot r_{\mathrm{PM}} \approx k_{\mathrm{SP}}r_n + m\theta - k_{\mathrm{SP}}r_p\cos(\varphi)$. We then deduce the SP field expression under reciprocal illumination $\mathbf{E}_{\mathrm{SP}}^{\parallel}(P) = \mathbf{E}_{\mathrm{SP}}^{\parallel,R}(P) + \mathbf{E}_{\mathrm{SP}}^{\parallel,L}(P)$ with

$$\begin{aligned}\mathbf{E}_{\mathrm{SP}}^{\parallel,S}(P) \propto \sum_n \frac{\mu}{4\pi\sqrt{2}}\sqrt{r_n}e^{ik_{\mathrm{SP}}r_n}\{(ie^{i\theta_p})^m J_m(V)\\ +(ie^{i\theta_p})^{m-2s_\pm}J_{m-2s_\pm}(V)\}\mathbf{S},\end{aligned} \tag{D5}$$

with J_l referring to the Bessel function of order l (signed integer number), $V = k_{\mathrm{SP}}r_p$, $\mathbf{S}$=$\mathbf{L}$ ($s_+ = 1$) or $\mathbf{R}$ ($s_- = -1$).

APPENDIX E: IN-PLANE PLASMONIC FIELDS BACK-REFLECTED ON THE DIPOLE SOURCE

Here, we treat the case of the SP field back-reflected to the dipole source. The SNOM configuration is as in Fig. 1(a).

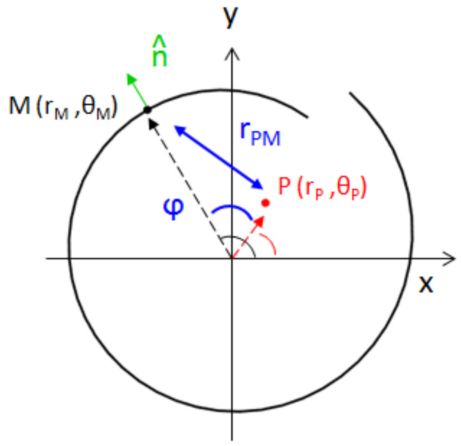

FIG. 10. Notations used for the derivation of the SP field.

In Fig. 5(b), we illustrate the different steps leading to the reflection of SP back to the dipole emitter: (1) The illumination SNOM probe located at position P is associated with an in-plane electric dipole $\boldsymbol{\mu} = \mu\hat{x}$ which excites propagating SP. (2) The SP scatter on the grooves at point M (see notations in Fig. 10). The radiated field writes

$$\mathbf{E}(M) \propto \frac{e^{ik_{\mathrm{SP}}\cdot r}}{\sqrt{|\,\mathbf{r}\,|}}(\boldsymbol{\mu}\cdot\hat{r})\hat{r} = \frac{e^{ik_{\mathrm{SP}}\cdot r}}{\sqrt{|\,\mathbf{r}\,|}}\mu\cos(\theta)\hat{r}. \tag{E1}$$

It induces in turn an in-plane dipole normal to the slit $(\mathbf{E}(M)\cdot\hat{n})\hat{n}$. This issue is well documented in the literature [31,35]. (3) The back-reflected in-plane SP field on emitter at position P is then derived by summing the contribution of all the point sources distributed along the grooves:

$$\mathbf{E}(P) \propto \int_{\theta_0}^{\theta_0+2\pi n} \frac{e^{ik_{\mathrm{SP}}\cdot r}}{r} (\mathbf{E}(M)\cdot\hat{n})(\hat{n}\cdot\hat{r})\hat{r}\,dl. \tag{E2}$$

We consider a tip position P at the vicinity of the spiral center. As $r_0 \gg \lambda_{\mathrm{SP}}$, it is suitable to approximate a spiral making n turns as n concentric rings of radius $r_n = r_0 + n \times \lambda_{\mathrm{SP}}$. Moreover, we assume $\hat{r} \approx \hat{n} \approx \mathbf{PM}/|\mathbf{PM}|$ and $k_{\mathrm{SP}}\cdot r_{\mathrm{PM}} \approx k_{\mathrm{SP}}r_n + m\theta - k_{\mathrm{SP}}r_p\cos(\varphi)$:

$$\begin{aligned}\mathbf{E}_{\mathrm{SP}}^{\parallel}(P) \propto \sum_n \frac{\mu}{2\sqrt{2}}\sqrt{r_n}e^{i2k_{\mathrm{SP}}r_n}\oint d\varphi\, e^{i2k_{\mathrm{SP}}r_p\cos(\varphi)}\\ \{(e^{2im\theta_p}e^{2im\varphi} + e^{2i(m+1)\theta_p}e^{2i(m+1)\varphi})\mathbf{R}\\ +(e^{2im\theta_p}e^{2im\varphi} + e^{2i(m-1)\theta_p}e^{2i(m-1)\varphi})\mathbf{L}\}.\end{aligned} \tag{E3}$$

We deduce the total back-reflected SP field $\mathbf{E}_{\mathrm{SP}}^{\parallel}(P) = \mathbf{E}_{\mathrm{SP}}^{\parallel,R}(P) + \mathbf{E}_{\mathrm{SP}}^{\parallel,L}(P)$ with

$$\begin{aligned}\mathbf{E}_{\mathrm{SP}}^{\parallel,S}(P) \propto \sum_n \frac{\mu}{4\pi\sqrt{2}}\sqrt{r_n}e^{i2k_{\mathrm{SP}}r_n}\{(ie^{i\theta_p})^{2m} J_{2m}(2V)\\ +(ie^{i\theta_p})^{2(m-s_-)}J_{2(m-s_\pm)}(2V)\}\mathbf{S},\end{aligned} \tag{E4}$$

with J_l referring to the Bessel function of order l (signed integer number), $V = k_{\mathrm{SP}}r_p$, $\mathbf{S} = \mathbf{L}$ ($s_+ = 1$), or $\mathbf{R}$ ($s_- = -1$). The OAM selection rule allows only Bessel modes with $l = 2m$ and $2(m - s_\pm)$ which differ from the measurements.

[1] M. Schaferling, D. Dregely, M. Hentschel, and H. Giessen, Phys. Rev. X **2**, 031010 (2012).

[2] A. Kinkhabwala, Z. Yu, S. Fan, Y. Avlasevich, K. Müllen, and W. Moerner, Nat. Photon. **3**, 654 (2009).

[3] G. Tkachenko and E. Brasselet, Nat. Commun. **5**, 3577 (2014).

[4] Y. Zhao, A. N. Askarpour, L. Sun, J. Shi, X. Li, and A. Alu, Nat. Commun. **8**, 14180 (2017).

[5] Y. Luo, C. Chi, M. Jiang, R. Li, S. Zu, Y. Li, and Z. Fang, Adv. Opt. Mater. **5**, 1700040 (2017).

[6] A. Pham, Q. Jiang, A. Zhao, J. Bellessa, C. Genet, and A. Drezet, ACS Photon. **4**, 2453 (2017).

[7] A. Pham, M. Berthel, Q. Jiang, J. Bellessa, S. Huant, C. Genet, and A. Drezet, Phys. Rev. A **94**, 053850 (2016).

[8] S. J. Yoo and Q.-H. Park, Phys. Rev. Lett. **114**, 203003 (2015).

[9] E. Hendry, T. Carpy, J. Johnston, M. Popland, R. Mikhaylovskiy, A. Lapthorn, S. Kelly, L. Barron, N. Gadegaard, and M. Kadodwala, Nat. Nanotechnol. **5**, 783 (2010).

[10] A. Canaguier-Durand and C. Genet, Phys. Rev. A **90**, 023842 (2014).

[11] R. Tullius, G. W. Platt, L. Khosravi Khorashad, N. Gadegaard, A. J. Lapthorn, V. M. Rotello, G. Cooke, L. D. Barron, A. O. Govorov, A. S. Karimullah, and M. Kadodwala, ACS Nano **11**, 12049 (2017).

[12] Y. Tang and A. E. Cohen, Phys. Rev. Lett. **104**, 163901 (2010).

[13] K. Y. Bliokh and F. Nori, Phys. Rev. A **83**, 021803 (2011).

[14] Y. Tang and A. E. Cohen, Science **332**, 333 (2011).

[15] A. Canaguier-Durand, J. A. Hutchison, C. Genet, and T. W. Ebbesen, New J. Phys. **15**, 123037 (2013).

[16] G. Colas des Francs, C. Girard, J.-C. Weeber, C. Chicane, T. David, A. Dereux, and D. Peyrade, Phys. Rev. Lett. **86**, 4950 (2001).

[17] C. Chicanne, T. David, R. Quidant, J. C. Weeber, Y. Lacroute, E. Bourillot, A. Dereux, G. Colas des Francs, and C. Girard, Phys. Rev. Lett. **88**, 097402 (2002).

[18] R. Carminati, A. Cazé, D. Cao, F. Peragut, V. Krachmalnicoff, R. Pierrat, and Y. De Wilde, Surf. Sci. Rep. **70**, 1 (2015).

[19] L. V. Poulikakos, P. Gutsche, K. M. McPeak, S. Burger, J. Niegemann, C. Hafner, and D. J. Norris, ACS Photon. **3**, 1619 (2016).

[20] R. Sapienza, T. Coenen, J. Renger, M. Kuttge, N. Van Hulst, and A. Polman, Nat. Mater. **11**, 781 (2012).

[21] C. I. Osorio, T. Coenen, B. J. Brenny, A. Polman, and A. F. Koenderink, ACS Photon. **3**, 147 (2015).

[22] S. Zu, Y. Bao, and Z. Fang, Nanoscale **8**, 3900 (2016).

[23] S. Hashiyada, T. Narushima, and H. Okamoto, ACS Photon. **5**, 1486 (2018).

[24] D. Cao, A. Cazé, M. Calabrese, R. Pierrat, N. Bardou, S. Collin, R. Carminati, V. Krachmalnicoff, and Y. De Wilde, ACS Photon. **2**, 189 (2015).

[25] N. Chevalier, Y. Sonnefraud, J. Motte, S. Huant, and K. Karrai, Rev. Sci. Instrum. **77**, 063704 (2006).

[26] K. Drexhage, J. Lumin. **1**, 693 (1970).

[27] M. Kuttge, E. J. R. Vesseur, A. F. Koenderink, H. J. Lezec, H. A. Atwater, F. J. García de Abajo, and A. Polman, Phys. Rev. B **79**, 113405 (2009).

[28] T. Coenen, E. J. R. Vesseur, A. Polman, and A. F. Koenderink, Nano Lett. **11**, 3779 (2011).

[29] M. Padgett, J. Courtial, and L. Allen, Phys. Today **57**(5), 35 (2004).

[30] Y. Gorodetski, A. Niv, V. Kleiner, and E. Hasman, Phys. Rev. Lett. **101**, 043903 (2008).

[31] Y. Gorodetski, A. Drezet, C. Genet, and T. W. Ebbesen, Phys. Rev. Lett. **110**, 203906 (2013).

[32] W. Brullot, M. K. Vanbel, T. Swusten, and T. Verbiest, Sci. Adv. **2**, e1501349 (2016).

[33] T. Han, S. Zu, Z. Li, M. Jiang, X. Zhu, and Z. Fang, Nano Lett. **18**, 567 (2017).

[34] S. Zu, T. Han, M. Jiang, F. Lin, X. Zhu, and Z. Fang, ACS Nano **12**, 3908 (2018).

[35] O. Mollet, G. Bachelier, C. Genet, S. Huant, and A. Drezet, J. Appl. Phys. **115**, 093105 (2014).

[36] M. Berthel, Q. Jiang, A. Pham, J. Bellessa, C. Genet, S. Huant, and A. Drezet, Phys. Rev. Appl. **7**, 014021 (2017).

[37] Z. Bomzon, G. Biener, V. Kleiner, and E. Hasman, Opt. Lett. **27**, 285 (2002).

[38] G. Milione, T. A. Nguyen, J. Leach, D. A. Nolan, and R. R. Alfano, Opt. Lett. **40**, 4887 (2015).

[39] F. Yue, D. Wen, J. Xin, B. D. Gerardot, J. Li, and X. Chen, ACS Photon. **3**, 1558 (2016).

[40] C.-H. Yang, Y.-D. Chen, S.-T. Wu, and A. Y.-G. Fuh, Sci. Rep. **6**, 31546 (2016).

[41] Y. C. Jun, K. C. Huang, and M. L. Brongersma, Nat. Commun. **2**, 283 (2011).

[42] H. Aouani, O. Mahboub, E. Devaux, H. Rigneault, T. W. Ebbesen, and J. Wenger, Nano Lett. **11**, 2400 (2011).

[43] J. A. Hachtel, R. B. Davidson, E. R. Kovalik, S. T. Retterer, A. R. Lupini, R. F. Haglund, B. J. Lawrie, and S. T. Pantelides, Opt. Lett. **43**, 927 (2018).

[44] K. D. Bonin, B. Kourmanov, and T. G. Walker, Opt. Express **10**, 984 (2002).

[45] P. Galajda and P. Ormos, Opt. Express **11**, 446 (2003).

[46] W.-Y. Tsai, J.-S. Huang, and C.-B. Huang, Nano Lett. **14**, 547 (2014).

[47] J. Wang, Photon. Res. **4**, B14 (2016).